Predicting large-Chern-number phases in a shaken optical dice lattice

Shujie Cheng,[1] Honghao Yin,[2] Zhanpeng Lu,[3] Chaocheng He,[1] Pei Wang,[1] and Gao Xianlong[1]
[1]*Department of Physics, Zhejiang Normal University, Jinhua 321004, China*
[2]*Department of Physics, Capital Normal University, Beijing 100048, China*
[3]*Institute of Theoretical Physics, Shanxi University, Taiyuan, Shanxi 030006, China*

(Received 30 January 2020; accepted 27 March 2020; published 27 April 2020)

With respect to the quantum anomalous Hall effect (QAHE), the detection of topological nontrivial large-Chern-number phases is an intriguing subject. Motivated by recent research on Floquet topological phases, this study proposes a periodic driving protocol to engineer large-Chern-number phases using the QAHE. Herein, spinless ultracold fermionic atoms are studied in a two-dimensional optical dice lattice with nearest-neighbor hopping and a Λ- or V-type sublattice potential subjected to a circular driving force. Results suggest that large-Chern-number phases exist with Chern numbers $C = -3$, which is consistent with the edge-state quasienergy spectra.

DOI: 10.1103/PhysRevA.101.043620

I. INTRODUCTION

In recent decades, since the discovery of the quantum Hall effect at low temperatures with strong magnetic fields [1], many studies have been conducted on the topological features of condensed matter [2–10]. The quantum anomalous Hall effect (QAHE) is a branch in this sustained field [8], and Chern insulators are one of the many insulators used in QAHE. Different from other topological insulators with time inversion symmetry [6], Chern insulators have topological features characterized by the Chern number (C), also known as the topological invariant, which was first proposed by Thouless-Kohmoto-Nightingale-den Nijs [2]. Moreover, $C \neq 0$ ($C = 0$) corresponds to the topological nontrivial (trivial) phase.

A paradigmatic Chern insulator system is the Haldane model [3]. Motivated by this model, some other lattice systems [11–23] are also predicted to contain topological nontrivial phases. Of these, large-Chern-number phases with QAHE have attracted widespread attention. In particular, some studies have considered long-range tunneling [11,12] or complex magnetic flux [21–23] to obtain topological phases with large Chern numbers. Further, large-Chern-number phases are theoretically predicted to appear in multilayered crystal structures [24–26]. In the field of interface transport, such intriguing phases are expected to enhance the performance of certain devices by reducing the channel resistance [27,28]. However, owing to the limitations of lattice structure, observing large-Chern-number phases in reality remains impossible. Even in topological nontrivial materials, the Chern numbers are mostly detected for $C = \pm 1$ [29–31]. Rarely, in the context of the photonic crystals [32], Chern numbers are measured up to $C = 4$ by introducing an external magnetic field.

Recently, the periodic driving protocol has been developed to generate the Floquet topological nontrivial phases with the QAHE. Its flexibility and versatility realize the possible designing of Floquet topological bands on demand; the scenario of Floquet topological states has been studied in many systems [33–51]. Moreover, the Floquet engineering is also recognized as an effective approach to realize the topological phases with large topological invariants [46–48,52,53]. This study aims to exploit a periodic driving protocol applied to a two-dimensional (2D) dice lattice [21–23,54–61] to realize large-Chern-number phases with the QAHE. To this end, spinless ultracold fermionic atoms were studied in a 2D optical dice lattice with nearest-neighbor hopping and a Λ- or V-type sublattice potential subjected to a circular driving force, $\boldsymbol{F}(t) = F[\cos(\omega t)\boldsymbol{e}_x - \sin(\omega t)\boldsymbol{e}_y]$ [33]. Here, F and ω are the amplitude and frequency of the driving force, respectively. The proposed protocol is based on two considerations: lattice geometry, which can be created using laser beams [62], and shaking [33], like the Haldane model [3]. We hope this system can be realized using similar experimental settings. After calculating the effective Hamiltonian, large-Chern-number phases are identified that contain Chern numbers $C = -3$; these results are consistent with the edge-state quasienergy spectra.

The remaining portions of this article are organized as follows. Section II describes the periodically driven dice model, which can be realized using the ultracold atoms trapped in a circularly shaken 2D dice optical lattice, presenting the effective Hamiltonian derived from the Floquet theorem in the process. Section III maps the effective Hamiltonian into the SU(3) system and numerically obtains the Chern-number phases; the bulk-edge correspondence is also analyzed. Finally, a brief summary is presented in Sec. IV.

II. PERIODICALLY DRIVEN DICE MODEL

Spinless ultracold fermionic atoms trapped in a shaken 2D dice optical lattice were considered, as depicted in Fig. 1(a). Three interpenetrating triangle sublattices were present: R, B, and G. This lattice geometry is similar to the Haldane model and can be formed using three retroreflected laser beams [62]. Through tight-binding approximation, the single-particle

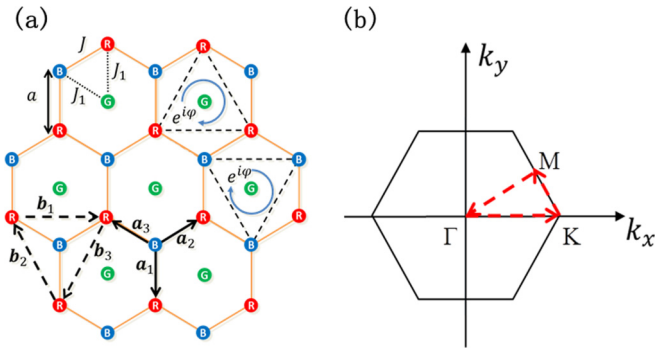

FIG. 1. (a) Schematic of the dice lattice with sublattice R (red), B (blue), and G (green). The Hamiltonian $\hat{H}_{\rm tun}$ possesses real tunneling matrix elements J between neighboring R and B sites and J_1 between neighboring G and R or B sites; the circular arrows show the tunneling between the same R and B sublattice sites with the tunneling phase $e^{i\varphi}$ ($\varphi = \frac{\pi}{2}$), which is contained in the effective Hamiltonian $\hat{\mathcal{H}}_{\rm eff}$. The vectors $\boldsymbol{a}_s$ ($s = 1, 2, 3$) connect the nearest-neighbor sites, whereas vectors $\boldsymbol{b}_s$ ($s = 1, 2, 3$) connect the next-nearest-neighbor R and B sites. In this paper, we choose $|\boldsymbol{a}_1| = |\boldsymbol{a}_2| = |\boldsymbol{a}_3| = a$ as units of length, thus, $|\boldsymbol{b}_s| = \sqrt{3}a = \sqrt{3}$. (b) The first Brillouin zone of the dice lattice. Γ, K, and M are high-symmetry points, connected by three dashed red arrows.

Hamiltonian of this shaken lattice system can be expressed as

$$\hat{H} = \hat{H}_{\rm tun} + \hat{H}_{\rm pot} + \hat{H}_{\rm dri}. \tag{1}$$

The first term $\hat{H}_{\rm tun}$ indicates the tunneling kinetics and can be expressed as

$$\begin{aligned}\hat{H}_{\rm tun} = &\sum_{\langle R_j, B_{j'}\rangle} J(\hat{c}^\dagger_{R_j}\hat{c}_{B_{j'}} + {\rm H.c.}) \\ &+ \sum_{\langle G_j, R_{j'}\rangle} J_1(\hat{c}^\dagger_{G_j}\hat{c}_{R_{j'}} + {\rm H.c.}) \\ &+ \sum_{\langle B_j, G_{j'}\rangle} J_1(\hat{c}^\dagger_{B_j}\hat{c}_{G_{j'}} + {\rm H.c.}),\end{aligned} \tag{2}$$

where the sum extending over the nearest-neighbor sites, R_j, B_j, and G_j, denotes the relevant sites of sublattice R, B, and G, respectively, and j denotes the corresponding site index; J denotes the tunneling parameter between one R site and one B site; J_1 denotes the tunneling parameter between one R and B site and one G site; and $\hat{c}_{R_j}$, $\hat{c}_{B_j}$, and $\hat{c}_{G_j}$ denote the corresponding fermionic annihilation operators.

The second term $\hat{H}_{\rm pot}$ describes a special on-site potential for atoms populating various sublattices:

$$\hat{H}_{\rm pot} = \epsilon_R \sum_{R_j} \hat{c}^\dagger_{R_j}\hat{c}_{R_j} + \epsilon_B \sum_{B_j} \hat{c}^\dagger_{B_j}\hat{c}_{B_j} + \epsilon_G \sum_{G_j} \hat{c}^\dagger_{G_j}\hat{c}_{G_j}, \tag{3}$$

where R and B sublattices have the same on-site potential $\epsilon_R = \epsilon_B \equiv \gamma_1\Delta$ and the G sublattice has the on-site potential of $\epsilon_G \equiv \gamma_2\Delta$, where Δ denotes the strength of the potential and γ_1 and γ_2 reflect how fast the tunable potential energy changes. If γ_1 and γ_2 are both positive and $\gamma_1 < \gamma_2$, the potential presents a Λ-type (V-type) structure when $\Delta > 0$ ($\Delta < 0$). The Λ-type (V-type) structure also appears in other cases where γ_1 and γ_2 are both completely or partially negative. Such on-site potential is different from that presented in previous studies on dice models [21–23]; it can be realized by tuning the single-beam lattice depths.

The third term $\hat{H}_{\rm dri}$ denotes the contribution of the circular periodic driving force in terms of the time-dependent on-site potential. This third term can be expressed as

$$\hat{H}_{\rm dri} = \sum_{\alpha_j} V(\boldsymbol{r}_{\alpha_j}, t)\hat{n}_{\alpha_j}, \tag{4}$$

where the sum runs over all lattice sites, $\boldsymbol{r}_{\alpha_j}$ denotes the lattice-site coordinates, $\alpha \in \{{\rm R}, {\rm G}, {\rm B}\}$ denotes the sublattice type, $\hat{n}_{\alpha_j} = \hat{c}^\dagger_{\alpha_j}\hat{c}_{\alpha_j}$ are the site number operators, and $V(\boldsymbol{r}_{\alpha_j}, t) = -\boldsymbol{r}_{\alpha_j}\cdot\boldsymbol{F}(t)$.

Herein, the case of strong driving is explored, wherein the amplitude F is scaled according to the driving frequency; i.e., $Fa \sim \hbar\omega$. Therefore, performing a gauge transformation before employing high-frequency approximation [49–51] is necessary. The gauge-dependent time-periodic unitary operator can be expressed as

$$\hat{U}(t) = \exp\left(-\frac{i}{\hbar}\sum_{\alpha_j}\int_0^t V(\boldsymbol{r}_{\alpha_j}, t)dt\cdot\hat{n}_{\alpha_j}\right). \tag{5}$$

Next, the transformed time-periodic Hamiltonian is determined (see the details provided in Appendix A):

$$\begin{aligned}\hat{H}_{\rm tra} &= \hat{U}^\dagger(t)\hat{H}\hat{U}(t) - i\hbar\hat{U}^\dagger(t)\frac{d}{dt}\hat{U}(t) \\ &= \hat{U}^\dagger(t)\hat{H}_{\rm tun}\hat{U}(t) + \hat{H}_{\rm pot}.\end{aligned} \tag{6}$$

The important features of the above time-dependent Hamiltonian $\hat{H}_{\rm tra}$ can be acquired from an effective time-independent Hamiltonian [49–51]. Before deriving the effective Hamiltonian, we first expand the Hamiltonian $\hat{H}_{\rm tra}$ as follows:

$$\hat{H}_{\rm tra} = \sum_{m=-\infty}^{\infty} \hat{\mathcal{H}}_m e^{im\omega t} + \hat{H}_{\rm pot}, \tag{7}$$

where $\hat{\mathcal{H}}_m$ denotes the Fourier components, modified by the Bessel functions $\mathcal{J}_m(\beta)$, with $\beta = Fa/(\hbar\omega)$ being the isotropic parameter (see the derivation in Appendix B). At high frequency, we then truncate the exact Hamiltonian $\hat{H}_{\rm tra}$ into finite orders [49–51] and get the effective Hamiltonian as follows

$$\hat{\mathcal{H}}_{\rm eff} = \hat{\mathcal{H}}_0 + \sum_{m=1}^{\infty}\frac{1}{m\hbar\omega}[\hat{\mathcal{H}}_m, \hat{\mathcal{H}}_{-m}] + \hat{H}_{\rm pot}, \tag{8}$$

where the higher-order terms involving $1/\hbar\omega$ are neglected in high-frequency driving cases.

In the following theoretical and numerical analysis, $\beta = 2.2$ and high frequency $\omega = 6J/\hbar$ are considered as an example; the terms in $\hat{\mathcal{H}}_m$ containing $\mathcal{J}_m(\beta)$ ($m \geqslant 3$) are negligible (see Fig. 2). Finally, the effective Hamiltonian $\hat{\mathcal{H}}_{\rm eff}$ of Eq. (8)

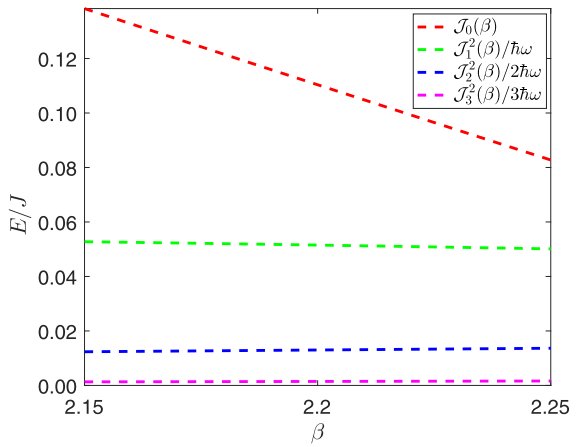

FIG. 2. Zero-order Bessel function (dashed red line), as well as the squares of the first-, second-, and third-order Bessel functions divided by the products of their order number and $\hbar\omega$ (dashed green, blue, and magenta lines, respectively) as a function of the isotropic parameter $\beta = Fa/(\hbar\omega)$.

is further expressed as

$$\begin{aligned}\hat{\mathcal{H}}_{\text{eff}} &= \hat{\mathcal{H}}_0 + \sum_{m=1,2} \frac{1}{m\hbar\omega}[\hat{\mathcal{H}}_m, \hat{\mathcal{H}}_{-m}] + \hat{H}_{\text{pot}} \\ &= \Bigg[\sum_{\langle R_j, B_{j'}\rangle} J_{rb}\hat{c}^\dagger_{R_j}\hat{c}_{B_{j'}} + \sum_{\langle B_j, G_{j'}\rangle} J_{bg}\hat{c}^\dagger_{B_j}\hat{c}_{G_{j'}} \\ &\quad + \sum_{\langle G_j, R_{j'}\rangle} J_{gr}\hat{c}^\dagger_{G_j}\hat{c}_{R_{j'}} + \sum_{\ll R_j, R_{j'}\gg} J_{rr}\hat{c}^\dagger_{R_j}\hat{c}_{R_{j'}} \\ &\quad + \sum_{\ll B_j, B_{j'}\gg} J_{bb}\hat{c}^\dagger_{B_j}\hat{c}_{B_{j'}} + \text{H.c.}\Bigg] + \epsilon_R \sum_{R_j} \hat{c}^\dagger_{R_j}\hat{c}_{R_j} \\ &\quad + \epsilon_B \sum_{B_j} \hat{c}^\dagger_{B_j}\hat{c}_{B_j} + \epsilon_G \sum_{G_j} \hat{c}^\dagger_{G_j}\hat{c}_{G_j}, \end{aligned} \tag{9}$$

where $\ll \cdots \gg$ denotes the next-nearest-neighbor relations, and the tunneling parameters are

$$\begin{aligned} J_{rb} &= J\mathcal{J}_0(\beta), \\ J_{bg/gr} &= J_1\mathcal{J}_0(\beta), \\ J_{rr/bb} &= \frac{\sqrt{3}}{2}e^{i\sigma\frac{\pi}{2}}\left(\frac{J^2 - J_1^2}{\hbar\omega}\right)\left[\mathcal{J}_1^2(\beta) - \frac{1}{2}\mathcal{J}_2^2(\beta)\right], \end{aligned} \tag{10}$$

with $\sigma = 1$ for clockwise tunneling and $\sigma = -1$ for counterclockwise tunneling.

III. CHERN NUMBER AND EDGE STATE

The infinite system is considered such that the translational symmetry is preserved. The $\hat{\mathcal{H}}_{\text{eff}}$ can be mapped into the SU(3) system, and the effective Bloch Hamiltonian [63,64] is expressed as

$$\hat{\mathcal{H}}_{\text{eff}}(\mathbf{k}) = I(\mathbf{k}) + \mathbf{d}(\mathbf{k}) \cdot \vec{\lambda}, \tag{11}$$

where $\mathbf{k}$ denotes a wave vector, $I(\mathbf{k})$ denotes a scalar, $\mathbf{d}(\mathbf{k})$ denotes an eight-dimensional real vector, and $\vec{\lambda}$ denotes a vector of Gell-Mann matrices [65]. In practice, the scalar $I(\mathbf{k})$ has no effect on the wave function; hence, the Chern number can only be determined by the coefficient vectors $\mathbf{d}(\mathbf{k})$. The discrete Fourier transformation is performed in the three-component basis $(\hat{c}_{\mathbf{k},R}, \hat{c}_{\mathbf{k},B}, \hat{c}_{\mathbf{k},G})^T$, where $\hat{c}_{\mathbf{k},\alpha} = \frac{1}{\sqrt{N}}\sum_{\alpha_j} e^{-i\mathbf{k}\cdot\boldsymbol{r}_{\alpha_j}}\hat{c}_{\alpha_j}$ (N is the unit-cell number), and the components of the vector $\mathbf{d}(\mathbf{k})$ are given as

$$\begin{aligned} &d_1 = J_{rb}\sum_s \cos(\mathbf{k}\cdot\boldsymbol{a}_s), \quad d_2 = J_{rb}\sum_s \sin(\mathbf{k}\cdot\boldsymbol{a}_s), \\ &d_4 = d_6 = J_{gr/bg}\sum_s \cos(\mathbf{k}\cdot\boldsymbol{a}_s), \\ &d_7 = -d_5 = J_{gr/bg}\sum_s \sin(\mathbf{k}\cdot\boldsymbol{a}_s), \\ &d_3 = -2J_{rr/bb}\sum_s \sin(\mathbf{k}\cdot\boldsymbol{b}_s), \quad d_8 = \frac{\gamma_1 - \gamma_2}{\sqrt{3}}\Delta, \end{aligned} \tag{12}$$

where we have set $a = 1$ for convenience and the six vectors $\boldsymbol{a}_s$ and $\boldsymbol{b}_s$ ($s = 1, 2, 3$), which are shown in Fig. 1(a), are displayed as

$$\begin{aligned} &\boldsymbol{a}_1 = \begin{pmatrix} 0 \\ -1 \end{pmatrix}, \quad \boldsymbol{a}_2 = \frac{1}{2}\begin{pmatrix} \sqrt{3} \\ 1 \end{pmatrix}, \quad \boldsymbol{a}_3 = \frac{1}{2}\begin{pmatrix} -\sqrt{3} \\ 1 \end{pmatrix}, \\ &\boldsymbol{b}_1 = \begin{pmatrix} \sqrt{3} \\ 0 \end{pmatrix}, \quad \boldsymbol{b}_2 = \frac{1}{2}\begin{pmatrix} -\sqrt{3} \\ 3 \end{pmatrix}, \quad \boldsymbol{b}_3 = -\frac{1}{2}\begin{pmatrix} \sqrt{3} \\ 3 \end{pmatrix}. \end{aligned} \tag{13}$$

Here, a slow-regulated Λ- or V-type potential with $\gamma_1 = \frac{1}{3}$ and $\gamma_2 = \frac{1}{2}$ is considered in the rest of the numerical calculations [66]. There are three bands in our system. For a given band, the corresponding Chern number is defined as [23,67,68]

$$C_n = \frac{1}{2\pi}\oint_{\partial\text{BZ}} \mathbf{A}_n(\mathbf{k}) \cdot d\mathbf{k}, \tag{14}$$

where ∂BZ denotes the boundary of the first Brillouin zone, $n \in \{1, 2, 3\}$ refers to the band index and the ascending order denotes the Floquet-band ranging from the lowest to the highest, $\mathbf{A}_n$ denotes the Berry connection with $\mathbf{A}_n = -i\langle\psi_n(\mathbf{k})|\nabla_{\mathbf{k}}|\psi_n(\mathbf{k})\rangle$, and $|\psi_n(\mathbf{k})\rangle$ denotes the corresponding eigenvector of $\hat{\mathcal{H}}_{\text{eff}}(\mathbf{k})$. In the following, we investigate the topological properties of the system at 1/3 filling and 2/3 filling [69], described by the quantities $C_{\frac{1}{3}}$ and $C_{\frac{2}{3}}$, respectively. The relationship of the Chern number for the topological property of the system at different fillings with the corresponding Chern numbers of the bands is given by $C_{\frac{1}{3}} = C_1$ and $C_{\frac{2}{3}} = C_1 + C_2$, respectively.

Figures 3(a1) and 3(a2) are the phase diagrams that exhibit variations of $C_{\frac{1}{3}}$ and $C_{\frac{2}{3}}$ as a function of the parameter Δ. In Fig. 3(a1), $C_{\frac{1}{3}}$ maintains a plateau within the interval of Δ (shown by the dotted red line). Therefore, the system is always in the topological nontrivial phase with $C_{\frac{1}{3}} = 1$. In Fig. 3(a2), useful phases appear when the system is at 2/3 filling (shown by the dotted blue lines). For small values of Δ, the system is in the topological nontrivial phase with $C_{\frac{2}{3}} = 1$. When Δ increases, the system undergoes a phase transition, entering a nontrivial large-Chern-number phase with $C_{\frac{2}{3}} = -2$. With the continued growth of Δ, the system becomes trivial with $C_{\frac{2}{3}} = 0$. To illustrate that these topological phases are

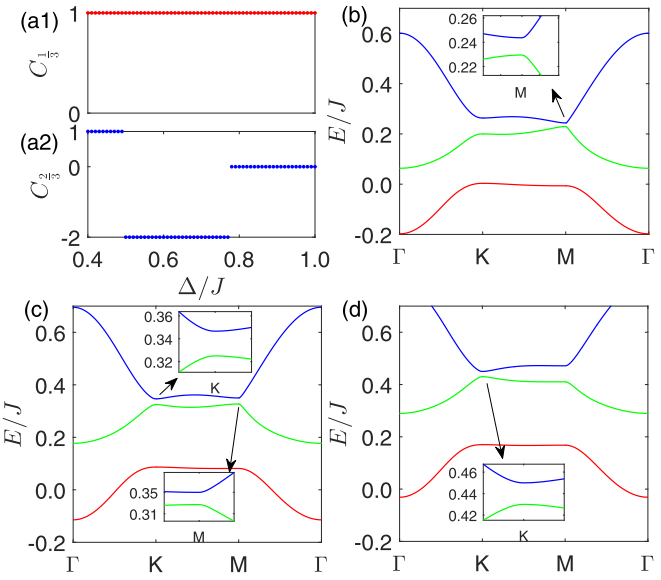

FIG. 3. (a1) Phase diagram of $C_{\frac{1}{3}}$ for the gapped lowest band (1/3 filling). The system always stays in the topological nontrivial phase with $C_{\frac{1}{3}} = 1$. (a2) The corresponding phase diagram of $C_{\frac{2}{3}}$ for the gapped lower two bands (2/3 filling). The system remains in the nontrivial phase with $C_{\frac{2}{3}} = -2$. (b)–(d) Gapped dispersions along the high-symmetry path Γ-K-M-Γ [see Fig. 1(b)] with parameters $\Delta = 0.4J$, $\Delta = 0.65J$, and $\Delta = 0.9J$, respectively. The other parameter used is $J_1 = 0.5J$. The insets are enlargements of the dispersions near the high-symmetry points indicated by the arrows.

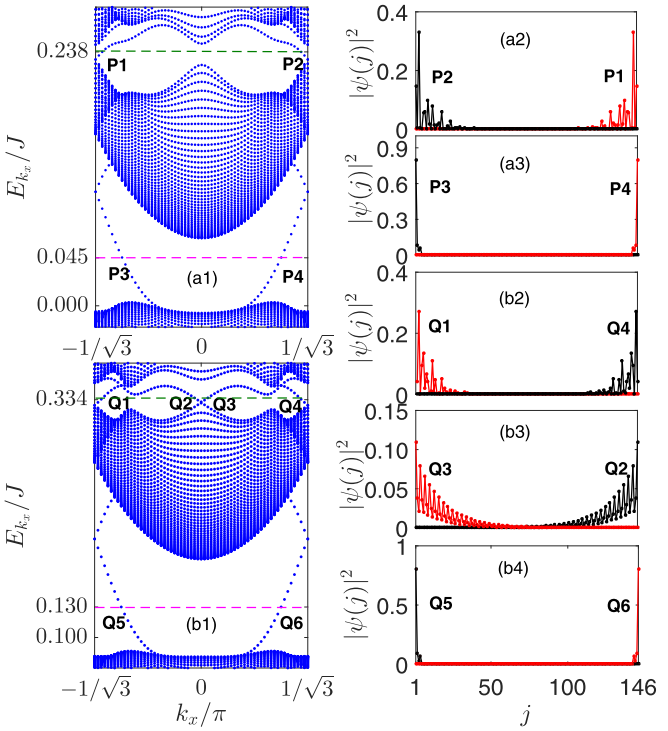

FIG. 5. Two edge-state quasienergy spectra when the cylindrical geometry which is shown in Fig. 4 is considered. E_{kx} denotes the quasienergy, and higher and lower values of E_k are not shown corresponding to the bulk states. (a1) $\Delta = 0.4J$. For 2/3 filling, E_{kx} is chosen as $0.238J$ (dashed green line). In this case, a pair of edge modes exist, labeled P1 and P2. For 1/3 filling, E_{kx} is chosen as $0.045J$ (dashed magenta line). Another pair of edge modes, labeled P3 and P4, also exist. (b1) $\Delta = 0.65J$. For 2/3 filling, E_{kx} is chosen as $0.334J$ (dashed green line). In this case, two pairs of edge modes, labeled Q1 and Q4 and Q2 and Q3 exist. For 1/3 filling, E_{kx} is chosen as $0.130J$ (dashed magenta line). Here, only one pair of edge modes, labeled Q5 and Q6, exist. The spatial density distributions of these paired edge modes are plotted in panels (a2) and (a3) and in panels (b2)–(b4), respectively. The distribution of the edge modes with positive group velocity are shown in red, whereas those of the edge modes with negative group velocity are shown in black. Results suggest that the edge states corresponding to the edge modes with opposite velocity are localized on different system boundaries, presenting the chiral symmetry. $N_s = 146$ has been considered in the numerical calculations.

gapped, we plot the dispersion relations of the bands at three chosen parameters ($\Delta = 0.4J$, $0.65J$, and $0.9J$) presented in Figs. 3(b), 3(c), and 3(d), respectively. In each diagram, the insets show the local amplification of the dispersion near the high-symmetry points [70]. As can be observed in the diagrams, no bands touch each other.

Here, the bulk-edge correspondence of the topological systems is discussed [45]. The Chern numbers of the filled bands are reflected by the chiral edge states observed in the edge states of the quasienergy spectrum. The chiral edge states are studied by considering a cylindrical geometry (shown in Fig. 4) with a periodic boundary condition in the x direction and an open boundary condition in the y direction (zig-zag edge). The lattice structure enclosed by the dashed box represents the periodic repeating unit, which contains N_s lattice sites. The Hamiltonian can be acquired via partial Fourier transformation and is parametrized by the good quantum number k_x.

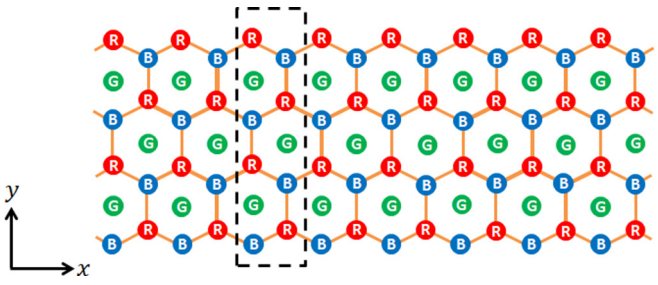

FIG. 4. Schematic of the cylindrical geometry with a periodic boundary condition in the x direction and an open boundary condition in the y direction (zig-zag edge). The lattice structure enclosed by the dashed box represents the periodic repeating unit, which contains N_s lattice sites.

By considering $N_s = 146$ and choosing $\Delta = 0.4J$ ($\Delta = 0.65J$), the edge-state quasienergy spectra are plotted as a function of k_x, as shown in Fig. 5(a1) [Fig. 5(b1)] where E_{kx} denotes the quasienergy [45,51]. Intuitively, when $\Delta = 0.4J$, the quasienergy spectrum intersects at $k_x = \pm\frac{\pi}{\sqrt{3}}$ both for 1/3 and 2/3 filling, implying a pair of chiral edge states regardless of the filling. Conversely, when $\Delta = 0.65J$, for 2/3 filling, the quasienergy spectrum intersects in two different manners, occurring at $k_x = \pm\frac{\pi}{\sqrt{3}}$ and $k_x = 0$. This indicates two pairs of chiral edge states. For 1/3 filling, only one pair of chiral edge states are observed. In Figs. 5(a1) and 5(b1), the dashed

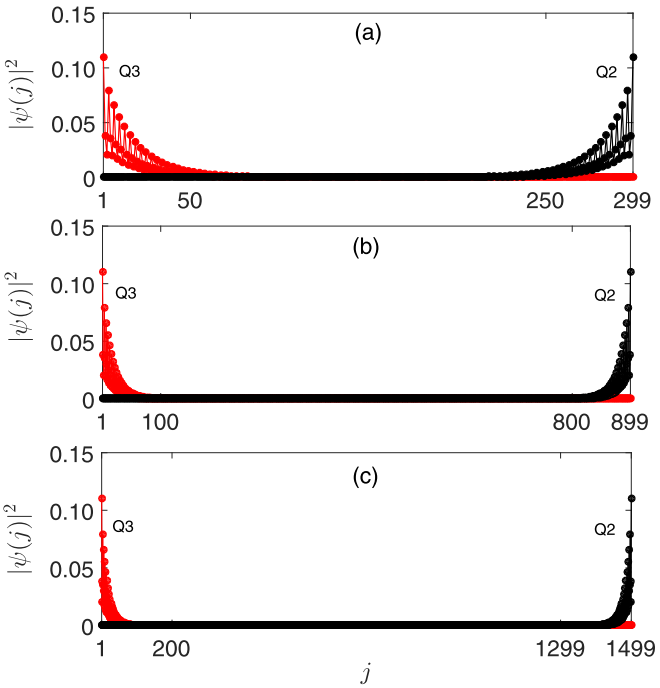

FIG. 6. The spatial density distributions of the edge modes Q2 and Q3 with larger N_s. The corresponding k_x stays the as same before. (a) $N_s = 299$. (b) $N_s = 899$. (c) $N_s = 1499$.

green and magenta lines represent the chosen quasienergies. P1–P4 and Q1–Q6 are the corresponding edge modes (labeled in black). To characterize the edge-state localization, the spatial density distributions of the corresponding edge modes are plotted in Figs. 5(a2) and 5(a3) and Figs. 5(b2)–5(b4), respectively. The distributions of the edge modes with positive group velocity are shown in red, whereas those of the edge modes with negative group velocity are shown in black. Label j is the index of the sites contained in the periodic repeating unit (see Fig. 4), and these sites are arranged in order of B-R-G-$\cdots$-B-R. Results suggest that edge states corresponding to the edge modes with opposite velocity are localized on different system boundaries, presenting the chiral symmetry.

Next, we will analyze the Chern numbers by the edge modes localized on the $j = N_s$ side. We have known that $C_{\frac{1}{3}} = 1$ for both $\Delta = 0.4J$ and $\Delta = 0.65J$. According to the bulk-edge correspondence principle [45], P4, P1, and Q6 with positive group velocity all correspond to $C = 1$, while Q2 and Q4 with negative group velocity both correspond to $C = -1$. Therefore, when $\Delta = 0.4J$, we have $C_1 = 1 - 0 = 1$ and $C_2 = 1 - 1 = 0$; when $\Delta = 0.65J$, $C_1 = 1 - 0 = 1$ and $C_2 = -1 + (-1) - 1 = -3$. These results are self-consistent with the phase diagrams in Figs. 3(a1) and 3(a2). We notice that there exists a finite-size effect on the edge modes Q1 and Q2. Then we test three spatial density distributions of the edge modes Q2 and Q3 with larger N_s in Fig. 6. The corresponding k_x stays the same as before but with more localized edge states when N_s is larger.

IV. SUMMARY

Herein, a periodic driving protocol was proposed to engineer large-Chern-number phases with the QAHE in a 2D periodically shaken optical dice model. Using the Floquet method, phase diagrams with 1/3 filling and 2/3 filling were obtained. We have analyzed the Chern numbers by the bulk-edge correspondence principle. The analytical results suggest that large-Chern-number phases exist with Chern numbers $C_2 = -3$, which is consistent with the edge-state quasienergy spectra.

ACKNOWLEDGMENTS

G.X. and S.C. acknowledge support from the NSFC under Grants No. 11835011 and No. 11774316.

APPENDIX A: DERIVATION OF EQ. (6)

The transformed Hamiltonian $\hat{H}_{\rm tra}$ in Eq. (6) can be expanded as

$$\begin{aligned}\hat{H}_{\rm tra} &= \hat{U}^\dagger(t)\hat{H}\hat{U}(t) - i\hbar\hat{U}^\dagger(t)\frac{d}{dt}\hat{U}(t)\\ &= \hat{U}^\dagger(t)\hat{H}_{\rm tun}\hat{U}(t) + \hat{U}^\dagger(t)\hat{H}_{\rm pot}\hat{U}(t)\\ &= \sum_{\langle R_j,B_{j'}\rangle} J(\hat{U}^\dagger(t)\hat{c}^\dagger_{R_j}\hat{U}(t)\hat{U}^\dagger(t)\hat{c}_{B_{j'}}\hat{U}(t) + \text{H.c.})\\ &\quad + \sum_{\langle G_j,R_{j'}\rangle} J_1(\hat{U}^\dagger(t)\hat{c}^\dagger_{G_j}\hat{U}(t)\hat{U}^\dagger(t)\hat{c}_{R_{j'}}\hat{U}(t) + \text{H.c.})\\ &\quad + \sum_{\langle B_j,G_{j'}\rangle} J_1(\hat{U}^\dagger(t)\hat{c}^\dagger_{B_j}\hat{U}(t)\hat{U}^\dagger(t)\hat{c}_{G_{j'}}\hat{U}(t) + \text{H.c.})\\ &\quad + \epsilon_R\sum_{R_j}\hat{U}^\dagger(t)\hat{n}_{R_j}\hat{U}(t) + \epsilon_B\sum_{B_j}\hat{U}^\dagger(t)\hat{n}_{B_j}\hat{U}(t)\\ &\quad + \epsilon_G\sum_{G_j}\hat{U}^\dagger(t)\hat{n}_{G_j}\hat{U}(t),\end{aligned} \tag{A1}$$

where $\hat{U}(t) = \exp(-\frac{i}{\hbar}\sum_{\alpha_j}\chi_{\alpha_j}(t)\cdot\hat{n}_{\alpha_j})$ with $\chi_{\alpha_j}(t) = \int_0^t V(\mathbf{r}_{\alpha_j},t)dt$.

Using the expansions presented above [49–51],

$$\begin{aligned}e^{i\hat{X}}\hat{Y}e^{-i\hat{X}} &= \hat{Y} + i[\hat{X},\hat{Y}] - \frac{1}{2}[\hat{X},[\hat{X},\hat{Y}]]\\ &\quad - \frac{i}{6}[\hat{X},[\hat{X},[\hat{X},\hat{Y}]]]\ldots\end{aligned} \tag{A2}$$

and considering the relation $[\hat{n}_{\alpha_j},\hat{n}_{\alpha'_{j'}}] = 0$, $\hat{H}_{\rm tra}$ was finally obtained, which can be expressed as

$$\begin{aligned}\hat{H}_{\rm tra} &= \sum_{\langle R_j,B_{j'}\rangle} J\left(e^{-i\frac{Fa}{\hbar\omega}\sin\left(\omega t+\theta^{R_j}_{B_{j'}}\right)}\hat{c}^\dagger_{R_j}\hat{c}_{B_{j'}} + \text{H.c.}\right)\\ &\quad + \sum_{\langle G_j,R_{j'}\rangle} J_1\left(e^{-i\frac{Fa}{\hbar\omega}\sin\left(\omega t+\theta^{G_j}_{R_{j'}}\right)}\hat{c}^\dagger_{G_j}\hat{c}_{R_{j'}} + \text{H.c.}\right)\\ &\quad + \sum_{\langle B_j,G_{j'}\rangle} J_1\left(e^{-i\frac{Fa}{\hbar\omega}\sin\left(\omega t+\theta^{B_j}_{G_{j'}}\right)}\hat{c}^\dagger_{B_j}\hat{c}_{G_{j'}} + \text{H.c.}\right)\\ &\quad + \hat{H}_{\rm pot},\end{aligned} \tag{A3}$$

where the angle $\theta_{\alpha'_{j'}}^{\alpha_j}$ is defined by the direction of the vector pointing from site $\alpha'_{j'}$ to its neighbor α_j,

$$\boldsymbol{r}_{\alpha_j} - \boldsymbol{r}_{\alpha'_{j'}} = a\left[\cos\left(\theta_{\alpha'_{j'}}^{\alpha_j}\right)\boldsymbol{e}_x + \sin\left(\theta_{\alpha'_{j'}}^{\alpha_j}\right)\boldsymbol{e}_y\right]. \tag{A4}$$

APPENDIX B: DERIVATION OF $\hat{\mathcal{H}}_m$

In this Appendix, Eq. (7) is derived. For convenience, we set

$$h = \exp\left[-i\frac{Fa}{\hbar\omega}\sin\left(\omega t + \theta_{\alpha'_{j'}}^{\alpha_j}\right)\right] = \exp\left[\frac{Fa}{\hbar\omega}\frac{e^{-i\sin\left(\omega t+\theta_{\alpha'_{j'}}^{\alpha_j}\right)} - e^{i\sin\left(\omega t+\theta_{\alpha'_{j'}}^{\alpha_j}\right)}}{2}\right]. \tag{B1}$$

By defining the isotropic parameter $\beta = Fa/(\hbar\omega)$ and using the Bessel function

$$\exp\left[\xi\frac{x - x^{-1}}{2}\right] = \sum_{\ell=-\infty}^{\infty}\mathcal{J}_\ell(\xi)x^\ell, \tag{B2}$$

we can obtain

$$h = \sum_{\ell=-\infty}^{\infty}\mathcal{J}_\ell(\beta)e^{-i\ell\left(\omega t+\theta_{\alpha'_{j'}}^{\alpha_j}\right)}, \qquad h^* = \sum_{\ell=-\infty}^{\infty}\mathcal{J}_\ell(\beta)e^{i\ell\left(\omega t+\theta_{\alpha'_{j'}}^{\alpha_j}\right)}. \tag{B3}$$

Upon performing Fourier transformation on h and h^*, the Fourier components of h and h^* are obtained as follows:

$$h_m = \mathcal{J}_{-m}(\beta)e^{im\theta_{\alpha'_{j'}}^{\alpha_j}}, \qquad (h^*)_m = \mathcal{J}_m(\beta)e^{im\theta_{\alpha'_{j'}}^{\alpha_j}}, \tag{B4}$$

where $\mathcal{J}_{-m}(\beta) = (-1)^m\mathcal{J}_m(\beta)$. Therefore, $\hat{\mathcal{H}}_m$ is obtained in Eq. (7) as follows:

$$\hat{\mathcal{H}}_m = \sum_{\langle R_j,B_{j'}\rangle} J\left(\mathcal{J}_{-m}(\beta)e^{im\theta_{B_{j'}}^{R_j}}\hat{c}_{R_j}^\dagger\hat{c}_{B_{j'}} + \mathcal{J}_m(\beta)e^{im\theta_{B_{j'}}^{R_j}}\hat{c}_{B_{j'}}^\dagger\hat{c}_{R_j}\right) + \sum_{\langle G_j,R_{j'}\rangle} J_1\left(\mathcal{J}_{-m}(\beta)e^{im\theta_{R_{j'}}^{G_j}}\hat{c}_{G_j}^\dagger\hat{c}_{R_{j'}} + \mathcal{J}_m(\beta)e^{im\theta_{R_{j'}}^{G_j}}\hat{c}_{R_{j'}}^\dagger\hat{c}_{G_j}\right) + \sum_{\langle B_j,G_{j'}\rangle} J_1\left(\mathcal{J}_{-m}(\beta)e^{im\theta_{G_{j'}}^{B_j}}\hat{c}_{B_j}^\dagger\hat{c}_{G_{j'}} + \mathcal{J}_m(\beta)e^{im\theta_{G_{j'}}^{B_j}}\hat{c}_{G_{j'}}^\dagger\hat{c}_{B_j}\right). \tag{B5}$$

[1] K. v. Klitzing, G. Dorda, and M. Pepper, New Method for High-Accuracy Determination of the Fine-Structure Constant Based on Quantized Hall Resistance, Phys. Rev. Lett. **45**, 494 (1980).

[2] D. J. Thouless, M. Kohmoto, M. P. Nightngale, and M. den Nijs, Quantized Hall Conductance in a Two-Dimensional Periodic Potential, Phys. Rev. Lett. **49**, 405 (1982).

[3] F. D. M. Haldane, Model for a Quantum Hall Effect without Landau Levels: Condensed-Matter Realization of the "Parity Anomaly", Phys. Rev. Lett. **61**, 2015 (1988).

[4] M. Z. Hasan and C. L. Kane, Colloquium: Topological insulators, Rev. Mod. Phys. **82**, 3045 (2010).

[5] X.-L. Qi and S.-C. Zhang, Topological insulators and superconductors, Rev. Mod. Phys. **83**, 1057 (2011).

[6] C. L. Kane and E. J. Mele, Z_2 Topological Order and the Quantum Spin Hall Effect, Phys. Rev. Lett. **95**, 146802 (2005).

[7] A. Kitaev, Periodic table for topological insulators and superconductors, AIP Conf. Proc. **1134**, 22 (2009).

[8] C.-K. Chiu, J. C. Y. Teo, A. P. Schnyder, and S. Ryu, Classification of topological quantum matter with symmetries, Rev. Mod. Phys. **88**, 035005 (2016).

[9] N. P. Armitage, E. J. Mele, and A. Vishwanath, Weyl and Dirac semimetals in three-dimensional solids, Rev. Mod. Phys. **90**, 015001 (2018).

[10] Y. Hatsugai, Chern Number and Edge States in the Integer Quantum Hall Effect, Phys. Rev. Lett. **71**, 3697 (1993).

[11] Y.-F. Wang, H. Yao, C.-D. Gong, and D. N. Sheng, Fractional quantum Hall effect in topological flat bands with Chern number two, Phys. Rev. B **86**, 201101 (2012).

[12] D. Sticlet and F. Piéchon, Distant-neighbor hopping in graphene and Haldane models, Phys. Rev. B **87**, 115402 (2013).

[13] K. Sun, H. Yao, E. Fradkin, and S. A. Kivelson, Topological Insulators and Nematic Phases from Spontaneous Symmetry Breaking in 2D Fermi Systems with a Quadratic Band Crossing, Phys. Rev. Lett. **103**, 046811 (2009).

[14] K. Ohgushi, S. Murakami, and N. Nagaosa, Spin anisotropy and quantum Hall effect in the kagomé lattice: Chiral spin state based on a ferromagnet, Phys. Rev. B **62**, R6065 (2000).

[15] Y. Xiao, V. Pelletier, P. M. Chaikin, and D. A. Huse, Landau levels in the case of two degenerate coupled bands: Kagomé lattice tight-binding spectrum, Phys. Rev. B **67**, 104505 (2003).

[16] H.-M. Guo and M. Franz, Topological insulator on the kagome lattice, Phys. Rev. B **80**, 113102 (2009).

[17] X.-P. Liu, W.-C. Chen, Y.-F. Wang, and C.-D. Gong, Topological quantum phase transitions on the kagomé and square–octagon lattices, J. Phys.: Condens. Matter **25**, 305602 (2013).

[18] C. Weeks and M. Franz, Topological insulators on the Lieb and perovskite lattices, Phys. Rev. B **82**, 085310 (2010).

[19] N. Goldman, D. F. Urban, and D. Bercioux, Topological phases for fermionic cold atoms on the Lieb lattice, Phys. Rev. A **83**, 063601 (2011).

[20] W.-F. Tsai, C. Fang, H. Yao, and J. Hu, Interaction-driven topological and nematic phases on the Lieb lattice, New J. Phys. **17**, 055016 (2015).

[21] G. Juzeliūnas and I. B. Spielman, Seeing topological order, Physics **4**, 99 (2011).

[22] N. Goldman, E. Anisimovas, F. Gerbier, P. Öhberg, I. B. Spielman, and G. Juzeliūnas, Measuring topology in a laser-coupled honeycomb lattice: From Chern insulators to topological semi-metals, New J. Phys. **15**, 013025 (2013).

[23] T. Andrijauskas, E. Anisimovas, M. Račiūnas, A. Mekys, V. Kudriašov, I. B. Spielman, and G. Juzeliūnas, Three-level Haldane-like model on a dice optical lattice, Phys. Rev. A **92**, 033617 (2015).

[24] H. Jiang, Z. Qiao, H. Liu, and Q. Niu, Quantum anomalous Hall effect with tunable Chern number in magnetic topological insulator film, Phys. Rev. B **85**, 045445 (2012).

[25] M. Barkeshli and X.-L. Qi, Topological Nematic States and Non-Abelian Lattice Dislocations, Phys. Rev. X **2**, 031013 (2012).

[26] S. Yang, Z.-C. Gu, K. Sun, and S. Das Sarma, Topological flat band models with arbitrary Chern numbers, Phys. Rev. B **86**, 241112 (2012).

[27] J. Wang, B. Lian, H. Zhang, Y. Xu, and S.-C. Zhang, Quantum Anomalous Hall Effect with Higher Plateaus, Phys. Rev. Lett. **111**, 136801 (2013).

[28] C. Fang, M. J. Gilbert, and B. A. Bernevig, Large-Chern-Number Quantum Anomalous Hall Effect in Thin-Film Topological Crystalline Insulators, Phys. Rev. Lett. **112**, 046801 (2014).

[29] S. A. Skirlo, L. Lu, and M. Soljačić, Multimode One-Way Waveguides of Large Chern Numbers, Phys. Rev. Lett. **113**, 113904 (2014).

[30] C.-Z. Chang, J. Zhang, X. Feng, J. Shen, Z. Zhang, M. Guo, K. Li, Y. Ou, P. Wei, L.-L. Wang, Z.-Q. Ji, Y. Feng, S. Li, X. Chen, J. Jia, X. Dai, Z. Fang, S.-C. Zhang, K. He, Y. Wang, L. Lu, X.-C. Ma, and Q.-K. Xue, Experimental observation of the quantum anomalous Hall effect in a magnetic topological insulator, Science **340**, 167 (2013).

[31] Y. Deng, Y. Yu, M. Z. Shi, Z. Guo, Z. Xu, J. Wang, X. H. Chen, and Y. Zhang, Quantum anomalous Hall effect in intrinsic magnetic topological insulator $MnBi_2Te_4$, Science **367**, 895 (2020).

[32] S. A. Skirlo, L. Lu, Y. Igarashi, Q. Yan, J. Joannopoulos, and M. Soljačić, Experimental Observation of Large Chern Numbers in Photonic Crystals, Phys. Rev. Lett. **115**, 253901 (2015).

[33] G. Jotzu, M. Messer, R. Desbuquois, M. Lebrat, T. Uehlinger, D. Greif, and T. Esslinger, Experimental realization of the topological Haldane model with ultracold fermions, Nature (London) **515**, 237 (2014).

[34] T. Oka and H. Aoki, Photovoltaic Hall effect in graphene, Phys. Rev. B **79**, 081406(R) (2009).

[35] T. Kitagawa, E. Berg, M. Rudner, and E. Demler, Topological characterization of periodically driven quantum systems, Phys. Rev. B **82**, 235114 (2010).

[36] N. H. Lindner, G. Refael, and V. Galitski, Floquet topological insulator in semiconductor quantum wells, Nat. Phys. **7**, 490 (2011).

[37] B. Dóra, J. Cayssol, F. Simon, and R. Moessner, Optically Engineering the Topological Properties of a Spin Hall Insulator, Phys. Rev. Lett. **108**, 056602 (2012).

[38] Y. T. Katan and D. Podolsky, Modulated Floquet Topological Insulators, Phys. Rev. Lett. **110**, 016802 (2013).

[39] D. Y. H. Ho and J. Gong, Quantized Adiabatic Transport In Momentum Space, Phys. Rev. Lett. **109**, 010601 (2012).

[40] D. Y. H. Ho and J. Gong, Topological effects in chiral symmetric driven systems, Phys. Rev. B **90**, 195419 (2014).

[41] A. Gómez-León and G. Platero, Floquet-Bloch Theory and Topology in Periodically Driven Lattices, Phys. Rev. Lett. **110**, 200403 (2013).

[42] A. Gómez-León, P. Delplace, and G. Platero, Engineering anomalous quantum Hall plateaus and antichiral states with ac fields, Phys. Rev. B **89**, 205408 (2014).

[43] F. Mei, J.-B. You, D.-W. Zhang, X. C. Yang, R. Fazio, S.-L. Zhu, and L. C. Kwek, Topological insulator and particle pumping in a one-dimensional shaken optical lattice, Phys. Rev. A **90**, 063638 (2014).

[44] S. Jana, P. Mohan, A. Saha, and A. Mukherjee, Tailoring metal insulator transitions and band topology via off-resonant periodic drive in an interacting triangular lattice, Phys. Rev. B **101**, 115428 (2020).

[45] M. S. Rudner, N. H. Lindner, E. Berg, and M. Levin, Anomalous Edge States and the Bulk-Edge Correspondence for Periodically Driven Two-Dimensional Systems, Phys. Rev. X **3**, 031005 (2013).

[46] T.-S. Xiong, J. B. Gong, and J.-H. An, Towards large-Chern-number topological phases by periodic quenching, Phys. Rev. B **93**, 184306 (2016).

[47] L. Zhou and J. Gong, Recipe for creating an arbitrary number of Floquet chiral edge states, Phys. Rev. B **97**, 245430 (2018).

[48] M. Umer, R. W. Bomantara, and J. Gong, Counter-propagating edge states in Floquet topological insulating phases, arXiv:2001.06972.

[49] S. Rahav, I. Gilary, and S. Fishman, Effective Hamiltonians for periodically driven systems, Phys. Rev. A **68**, 013820 (2003).

[50] N. Goldman and J. Dalibard, Periodically Driven Quantum Systems: Effective Hamiltonians and Engineered Gauge Fields, Phys. Rev. X **4**, 031027 (2014).

[51] A. Eckardt, Colloquium: Atomic quantum gases in periodically driven optical lattices, Rev. Mod. Phys. **89**, 011004 (2017).

[52] J. Vidal, R. Mosseri, and B. Douçot, Aharonov-Bohm Cages in Two-Dimensional Structures, Phys. Rev. Lett. **81**, 5888 (1999).

[53] B. Dey and T. K. Ghosh, Floquet topological phase transition in $\alpha - \mathcal{T}_3$ lattice, Phys. Rev. B **99**, 205429 (2019).

[54] D. Bercioux, D. F. Urban, H. Grabert, and W. Häusler, Massless Dirac-Weyl fermions in a $\mathcal{T}_3$ optical lattice, Phys. Rev. A **80**, 063603 (2009).

[55] G. Möller and N. R. Cooper, Correlated Phases of Bosons in the Flat Lowest Band of the Dice Lattice, Phys. Rev. Lett. **108**, 045306 (2012).

[56] M. Rizzi, V. Cataudella, and R. Fazio, Phase diagram of the Bose-Hubbard model with $\mathcal{T}_3$ symmetry, Phys. Rev. B **73**, 144511 (2006).

[57] A. A. Burkov and E. Demler, Vortex-Peierls States in Optical Lattices, Phys. Rev. Lett. **96**, 180406 (2006).

[58] D. Bercioux, N. Goldman, and D. F. Urban, Topology-induced phase transitions in quantum spin Hall lattices, Phys. Rev. A **83**, 023609 (2011).

[59] F. Wang and Y. Ran, Nearly flat band with Chern number $C = 2$ on the dice lattice, Phys. Rev. B **84**, 241103 (2011).

[60] Y.-R. Chen, Y. Xu, J. Wang, J.-F. Liu, and Z. Ma, Enhanced magneto-optical response due to the flat band in nanoribbons made from the $\alpha - T_3$ lattice, Phys. Rev. B **99**, 045420 (2019).

[61] R. Soni, N. Kaushal, S. Okamoto, and E. Dagotto, Flat bands and edge currents in dice-lattice ladders, arXiv:1911.11267.

[62] L. Tarruell, D. Greif, T. Uehlinger, G. Jotzu, and T. Essinger, Creating, moving and merging Dirac points with a Fermi gas in a tunable honeycomb lattice, Nature (London) **483**, 302 (2012).

[63] G. Khanna, S. Mukhopadhyay, R. Simon, and N. Mukunda, Geometric phases for SU(3) representations and three level quantum systems, Ann. Phys. **253**, 55 (1997).

[64] R. Barnett, G. R. Boyd, and V. Galitski, SU(3) Spin-Orbit Coupling in Systems of Ultracold Atoms, Phys. Rev. Lett. **109**, 235308 (2012).

[65] H. Georgi, Lie Algebras In *Particle Physics: From Isospin To Unified Theories* (Benjamin/Cummings, Reading, MA, 1982).

[66] Other values of γ_1 and γ_2 are tried with similar conclusions.

[67] N. Goldman, G. Juzeliūnas, P. Öhberg, and I. B. Spielman, Light-induced gauge fields for ultracold atoms, Rep. Prog. Phys. **77**, 126401 (2014).

[68] P. Wang, M. Schmitt, and S. Kehrein, Universal nonanalytic behavior of the Hall conductance in a Chern insulator at the topologically driven nonequilibrium phase transition, Phys. Rev. B **93**, 085134 (2016).

[69] We call the case that the lowest band filled $1/3$ filling, and the case that the lowest two bands filled $2/3$ filling.

[70] W. Setyawan and S. Curtarolo, High-throughput electronic band structure calculations: Challenges and tools, Comput. Mater. Sci. **49**, 299 (2010).